Structure and permeation mechanism of a mammalian urea transporter

Elena J. Levin[a,1], Yu Cao[a,1], Giray Enkavi[b], Matthias Quick[c], Yaping Pan[a], Emad Tajkhorshid[b,2], and Ming Zhou[a,2]

[a]Department of Physiology and Cellular Biophysics, College of Physicians and Surgeons, Columbia University, 630 West 168th Street, New York, NY 10032; [b]Center for Biophysics and Computational Biology, Department of Biochemistry, College of Medicine, and Beckman Institute for Advanced Science and Technology, University of Illinois at Urbana-Champaign, Urbana, IL 61801; and [c]Department of Psychiatry and Center for Molecular Recognition, Columbia University, 650 West 168th Street, New York, NY 10032

Edited by Christopher Miller, HHMI, Brandeis University, Waltham, MA, and approved June 1, 2012 (received for review May 3, 2012)

As an adaptation to infrequent access to water, terrestrial mammals produce urine that is hyperosmotic to plasma. To prevent osmotic diuresis by the large quantity of urea generated by protein catabolism, the kidney epithelia contain facilitative urea transporters (UTs) that allow rapid equilibration between the urinary space and the hyperosmotic interstitium. Here we report the first X-ray crystal structure of a mammalian UT, UT-B, at a resolution of 2.36 Å. UT-B is a homotrimer and each protomer contains a urea conduction pore with a narrow selectivity filter. Structural analyses and molecular dynamics simulations showed that the selectivity filter has two urea binding sites separated by an approximately 5.0 kcal/mol energy barrier. Functional studies showed that the rate of urea conduction in UT-B is increased by hypoosmotic stress, and that the site of osmoregulation coincides with the location of the energy barrier.

channels | membrane proteins | renal physiology | osmosensing

Urea transporters (UTs) are a family of integral membrane proteins that mediate the rapid and passive diffusion of urea down its concentration gradient. In mammals, UTs are expressed in a wide variety of tissues, but their function is best understood in the kidney where they contribute to maintaining the high interstitial urea concentration necessary to limit the rate of water loss (1–3). During periods of water deprivation, the kidney develops a steep urea gradient from the cortex at 5–8 mM (roughly the concentration present in plasma), to as much as 100-fold higher in the inner medulla (4). While active transport of ions out of the renal tubules is currently thought to provide the main energetic driving force for creating this gradient, passive transport through UTs also contributes through a countercurrent exchange mechanism that slows the diffusion of urea away from the inner medulla (5). Additionally, UTs expressed in the inner medullary collecting ducts allow the rapid equilibration of urea between the lumen and the interstitium, preventing water loss driven by the high concentration of urea present in the urine (6). The importance of UTs in the urinary concentrating mechanism has been verified by extensive knockout studies in mice (7–11), and mutations in UT genes in humans have been linked to variations in blood pressure (12) and the incidence of bladder cancer (13, 14).

Two genes encode for UTs in mammals: *slc14a1* and *slc14a2*. The *slc14a1* gene contains a single UT domain encoding the protein UT-B, which is expressed in the vasa recta, the nephron's primary blood vessel, as well as in a number of other tissues including erythrocytes, heart, colon, and the brain (15). In contrast, the *slc14a2* gene, which encodes UT-A, contains two UT domains in tandem, produces a variety of isoforms via alternative splicing, and is regulated by phosphorylation induced by the antidiuretic hormone vasopressin (16–18). Both UTs facilitate permeation of urea down its concentration gradient, and although the UTs were originally predicted to be transporters, measurements of single-channel flux rates ranging from 10^4–10^6 urea molecules/s (19, 20) were more consistent with a channel-like mechanism. This was confirmed with the solution of the structure of a bacterial homolog (21), dvUT, which forms a trimer with a continuous membrane-spanning pore at the center of each protomer. However, it remained unclear how similar this structure was to that of the mammalian UTs, and the details of the permeation mechanism were unknown. To answer these questions, we solved the structure of a mammalian UT-B and investigated the permeation mechanism with molecular dynamics simulations and functional studies of UT-B mutants.

Results

The Crystal Structure of Bovine UT-B. After screening several mammalian UT-A and UT-B homologs, we found that UT-B from both *Bos taurus* and *Homo sapiens* could be overexpressed in insect cells and purified in detergent-solubilized form. The bovine UT-B homolog produced small crystals, whose size and quality could be improved by subjecting the protein to partial proteolysis with trypsin. The structure was solved to a resolution of 2.36 Å by molecular replacement using the structure of dvUT (21) (PDB id 3K3F) as a search model. The final model contains three UT-B protomers with residues 31 to 376 resolved and 23 complete and partially ordered detergent and lipid molecules in the asymmetric unit (Table S1).

Bovine UT-B forms a trimer (Fig. 1*A*) with a total buried surface area of approximately 3500 $Å^2$. Purified human UT-B ran at a similar position as the bovine homolog on a size-exclusion column, suggesting that it is also a trimer (Fig. S1). Furthermore, the trimer interface is formed by equivalent helices in both the dvUT and UT-B structures (Fig. S2*A*), indicating that this quaternary structure may be conserved across the UT family. At the center of the trimer interface is a large cavity sealed off from the solvent, which is packed with partially ordered lipid or detergent molecules whose electron density is not of sufficient quality for identification. The individual protomers have the same overall fold as dvUT, and the root mean square deviation for main chain atoms in the transmembrane region is 0.7 Å (Fig. S2*B*). The UT fold contains two homologous halves with opposite orientations in the membrane, likely the product of duplication of an ancestral gene (22, 23), which give the structure an internal pseudo-twofold symmetry axis. Each half contains five transmembrane helices (T1a-5a and T1b-5b) and one tilted reentrant helix spanning roughly half of the membrane (Pa and Pb, Fig. 1*B*,

Author contributions: E.J.L., Y.C., E.T., and M.Z. designed research; E.J.L., Y.C., G.E., M.Q., and Y.P. performed research; E.J.L., Y.C., G.E., M.Q., Y.P., E.T., and M.Z. analyzed data; and E.J.L., E.T., and M.Z. wrote the paper.

The authors declare no conflict of interest.

This article is a PNAS Direct Submission.

Data deposition: The atomic coordinates and structure factors have been deposited in the Protein Data Bank, www.pdb.org (PDB ID code 4EZC and 4EZD).

[1]E.J.L. and Y.C. contributed equally to this work.

[2]To whom correspondence may be addressed. E-mail: mz2140@columbia.edu or emad@life.illinois.edu.

This article contains supporting information online at www.pnas.org/lookup/suppl/doi:10.1073/pnas.1207362109/-/DCSupplemental.

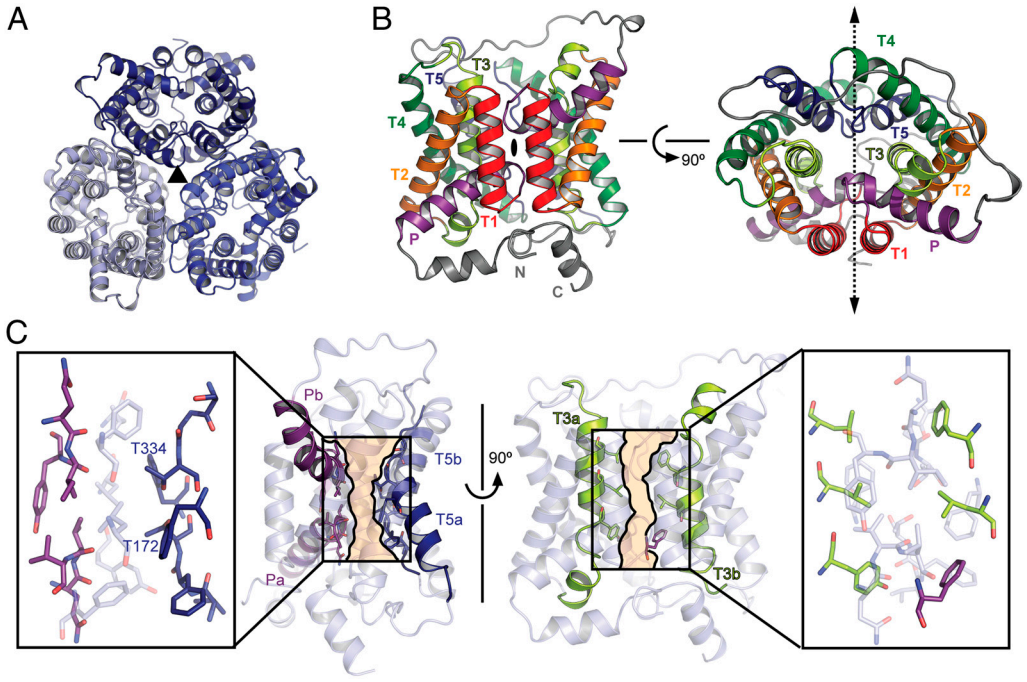

Fig. 1. *2.36 Å crystal structure of bovine UT-B.* (*A*) The UT-B trimer viewed from the extracellular side of the membrane, with the threefold symmetry axis (black triangle) labeled. (*B*) The structure of a UT-B protomer as viewed from within the plane of the membrane (*Left*) and from the extracellular side of the membrane (*Right*). The transmembrane helices are colored in pseudo-symmetry-related pairs. (*C*) The urea permeation pathway is shown viewed from two perpendicular orientations, with cross-sections of the wide (*Left*) and narrow (*Right*) dimensions of the pore marked in beige. *Insets* show residues lining the pore within the regions marked by black rectangles.

Fig. S2*C*). The largest difference between UT-B and dvUT lies in the orientation of a short amphipathic helix on the N-terminus; however, this helix forms key crystal contacts in the structure of dvUT (Fig. S3), and thus may be perturbed from its native conformation in the bacterial structure.

An amphipathic membrane-spanning pore is formed at the interface of the two halves in each protomer and is lined by residues from conserved urea signature sequences (22) (Fig. S4 *A* and *B*). The selectivity filter can be divided into three regions: the S_o and S_i sites, which are rectangular in cross-section with evenly-spaced arrays of carbonyl and side-chain oxygen atoms lining one side of the pathway (the oxygen ladders); and S_m, a constricted region at the center of the filter which is hydrophobic save for a pair of pseudo-symmetry related threonine residues (Figs. 1*C*, and 2 *A* and *B*). The largest difference between the pore-lining residues in the bacterial and mammalian UTs is a phenylalanine-to-glycine mutation in the S_o site (position 230 in the mammalian structure), although this mutation appears to be compensated by a leucine residue on helix TM3a, whose side chain takes the place of the aromatic ring (Fig. S4*C*).

Ligand Binding Sites in the Selectivity Filter. We then attempted to solve a substrate-bound structure to visualize interactions between the substrate and the protein. Since efforts to obtain high-resolution crystals of the protein bound to urea were unsuccessful, we cocrystallized UT-B with 20 mM selenourea, which is chemically similar to urea and has the additional advantage of producing a strong anomalous signal. The structure of UT-B in complex with selenourea was solved by molecular replacement to a resolution of 2.5 Å with a dataset collected at a wavelength corresponding to the *K*-absorption edge of selenium (Table S1). The protein's conformation is unchanged, but two wedge-shaped densities consistent with selenourea appear in the S_o and S_i sites (Fig. 2*A*), coincident with two >13.0σ anomalous difference peaks that render the identity and orientation of the selenourea molecules unambiguous (Fig. 2*B*). Both substrates are oriented to form hydrogen bonds between their amide hydrogens and the oxygen ladders. However, the two sites are not pseudo symmetrically equivalent: The S_o site selenourea is positioned to straddle the outermost "rung" of the oxygen ladder, while the S_i site ligand is level with the middle carbonyl. This suggests that as urea moves through the S_o and S_i regions, it may have more than one stable position. The substitution of one of the phenylalanines in the S_o site, F190 in the bacterial structure, with a leucine residue at position 127 in the mammalian structure does not appear to have affected the suitability of this region as binding site, implying that aromatic residues are not specifically necessary for stabilizing the bound substrate. Intriguingly, the S_m site, which appears to have a suitable configuration of hydrogen bond donors and acceptors for urea binding, was unoccupied in the selenourea-bound UT-B structure as well as in a previous dvUT structure bound to the urea analog 1,3-dimethylurea (21).

In order to provide a more dynamic description of the mechanism and pathway of permeation with the natural substrate, urea, and to characterize the energetics associated with the process, we then employed molecular dynamics simulations. Umbrella sampling (24) was used to reconstruct the potential of mean force (PMF) associated with urea permeation through UT-B using the projection of the carbon atom of urea along the pore axis as the reaction coordinate. Urea permeates the channel with minimal rotation around the channel axis (Movie S1), a configuration imposed by the hydrogen bonding pattern with the oxygen ladder in an otherwise hydrophobic pore. The projection of the dipole moment of urea on the pore axis exhibits a clear pattern of alternation reflecting its stepwise transition between adjacent, hydrogen-bonding sites (Fig. S5*A*). This "rocking" motion allows urea to permeate through the channel without causing significant perturbation, confirming that UTs indeed operate by a channel-like mechanism (Movie S1).

The PMF shows two almost symmetric pairs of energy minima in the S_o and S_i regions (Fig. 2*C*, Fig. S5*B*). Two of these minima, one in each of the S_o and S_i sites, agree well with the observed ligand positions in the selenourea-bound structure (Fig. 2*C*, yellow circles). In contrast, the S_m site is characterized by a

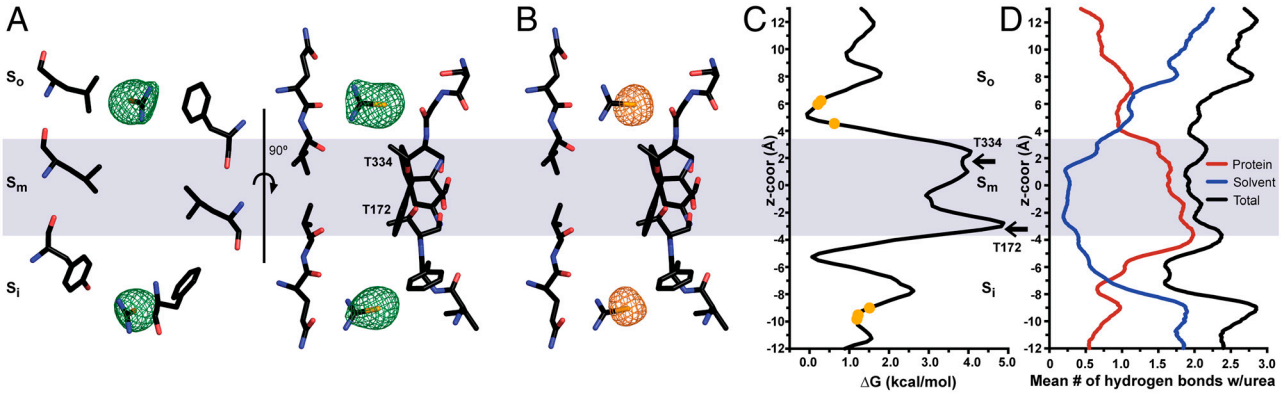

Fig. 2. *Energetics and binding sites in the UT-B pore.* (*A–B*) F_o-F_c density calculated without ligands in the model (*A*), and anomalous difference density (*B*) are shown in the pore of the selenourea/UT-B structure along with key selectivity filter residues. The maps are contoured at 3 and 5σ, respectively. (*C*) MD simulations were used to reconstruct the potential of mean force of urea permeation through the UT-B pore. The yellow circles indicate the *z*-coordinates of the central carbons of bound selenourea in the three subunits of the crystal structure, black arrows indicate the *z*-coordinates of the S_m site threonine CG atoms averaged over the three subunits. (*D*) The number of hydrogen bonds between urea and the protein (red), water molecules (blue), or both (black) averaged over the MD simulations as a function of the reaction coordinate.

large energy barrier with a maximum ΔG of approximately 5.0 kcal/mol with respect to the S_i or S_o sites. We attribute the energy barrier at the S_m site primarily to the desolvation cost in this region; while in the S_o and S_i sites, urea is only partially dehydrated and maintains on the average approximately 1.5–2.0 hydrogen bonds with water molecules (Fig. 2*D*), whereas upon entering the S_m site it becomes completely dehydrated.

Role of the S_m Site in Permeation and Modulation. To verify this observation experimentally, we mutated an S_m site threonine to valine to further diminish the ability of the protein to compensate for the dehydration penalty of urea in that region. The function of the mutant channels was measured by reconstituting them into liposomes preloaded with urea and using a fluorescence-based assay to measure the rate of urea efflux (25). The wild-type channel was functional and increased the initial rate over that of control liposomes by over 20-fold (Fig. 3*A*). As predicted by the simulations, the rate of urea efflux for the T334V mutant was close to that of control liposomes. In contrast, the T172S and T334S mutations, which conserve hydrogen bonding, had little effect on the rate of urea flux even when combined (Fig. 3*B*). Equilibrium MD simulations of both the T172V/T334V and the T172S/T334S double mutants show that in addition to increasing the hydrophobicity of the S_m site, loss of the hydrogen bond between T172 and T334 in the valine mutants causes a rotation of V334 towards the pore, so that the hydrophobic side chain obstructs the S_m site to the degree that even water molecules are not able to readily cross this region (Fig. S6).

These results indicate that the UT selectivity filter does not form a contiguous series of binding sites, but instead contains a substantial energy barrier at the highly conserved S_m site. We speculated that relatively small changes in the conformation of the pore at the S_m site could have substantial effects on the rate of transport, and that S_m could potentially serve as a site to regulate the rate of urea permeation. Given that the physiological role of UTs is closely linked to osmoregulation, we tested the channel for sensitivity to osmotic stress by measuring radiolabeled urea uptake into oocytes expressing UT-B in isotonic, hypotonic, and hypertonic buffer (Fig. 3*C*). Oocytes expressing wild type UT-B experienced an approximately twofold increase in urea uptake in the hypotonic buffer relative to uptake under isotonic conditions, indicating sensitivity of the channel to osmotic stress. In contrast, the hypertonic buffer did not alter the rate of urea uptake. This suggests that the effect cannot be attributed solely to cotransport of urea with water, since in that case reversing the direction of water permeation would be expected to have an inhibitory effect. To test whether the S_m site was involved in the response of the channel to hypoosmotic stress, we also measured uptake for oocytes expressing the T172S/T334S double mutant under identical conditions. Consistent with the results of the liposome assay, the T172S/T334S mutant had a similar basal rate of urea permeation to the wild type channel under isotonic conditions. However, unlike the wild type channel, the

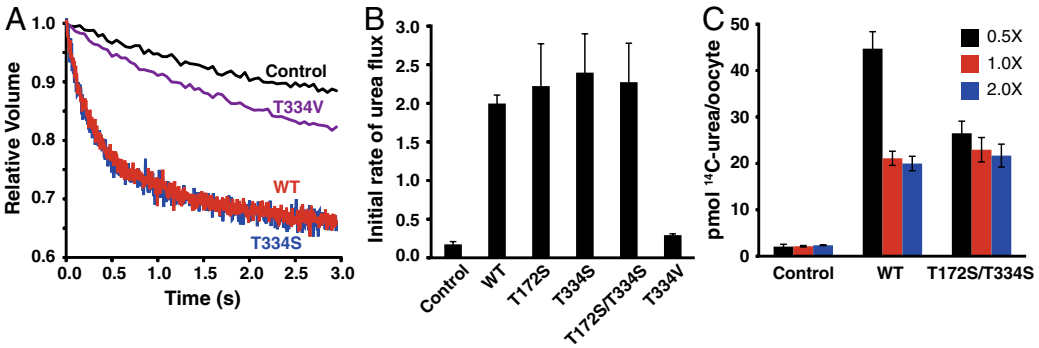

Fig. 3. Role of S_m site residues in urea flux and osmosensing. (*A*) Averaged, background-corrected traces showing the change in fluorescence over time from quenching of entrapped dye in WT (red), T334V (violet), and T334S (blue) UT-B-containing proteoliposomes and control liposomes (black), driven by urea efflux, scaled to the theoretical change in volume. (*B*) Initial rates of urea efflux calculated from these curves and for additional mutants. Errors bars are standard deviations from three or four experiments. (*C*) ^{14}C-labelled urea uptake in WT or T172S/T334S UT-B mRNA-injected oocytes or in control oocytes after 5 min placed in ND-96 buffer at 0.5, 1.0, and 2.0-fold concentration.

T172S/T334S mutant did not exhibit an increase in the rate of transport in a hypotonic buffer (Fig. 3*C*, Fig. S7). These results demonstrate a potential mechanism for modulation of UT-B function and support the hypothesis that the rate of urea conduction is regulated at the constricted region, the S_m site, in the selectivity filter.

Discussion

UT-B is a trimeric urea channel whose rate of permeation appears to be modulated by osmotic pressure. The energy barrier at S_m in UT-B is reminiscent of that observed in the ar/R motifs of aquaporins (26–28) or the conserved pore histidines in ammonia channels (29, 30). The aquaporin ar/R motifs are known to be crucial for selectivity; the height of this barrier largely determines the difference between the canonical aquaporins that permeate only water and the comparatively promiscuous aquaglyceroporins (31–33). The S_m site may likely play an analogous role in UTs, and confer the ability to block the flux of charged species like protons, ammonium and guanidinium that has been measured previously for other UT homologs (19, 34, 35). While the S_m site does not contain charged residues to exclude ions through electrostatic repulsion, as the ar/R motifs do (36), it is relatively hydrophobic and too narrow to permit a hydration sphere; the helix dipoles may also help repel anions. The hydrophobicity of the S_m site likely accounts for urea transporters' lower rate of water conduction relative to the canonical aquaporins (37), despite the strong structural similarities of the pores between the two families.

One notable difference between the UT-B and UT-A orthologs is that the latter is upregulated by the antidiuretic hormone vasopressin via phosphorylation of multiple sites on its long cytoplasmic N-terminus (16). Some of this increase in activity can be accounted for by increased localization of UT-A in the plasma membrane (38), but there is also evidence for an increase in urea transport activity that occurs on a more rapid time scale than the rate of accumulation of UT-A in the plasma membrane, possibly due to modulation of UT activity through phosphorylation of proteins already present at the cell surface (39). Given the high conservation of pore-lining residues between UT-B and UT-A, it is tempting to consider the possibility that the S_m site barrier is also present in UT-A, but with phosphorylation rather than osmotic stress as the trigger for modulation.

In the kidney, UT-B is expressed in the descending vasa recta, the blood vessel that supplies the nephron. In addition to providing the nephron with blood, the vasa recta is thought to play a role in the counter-current exchange mechanism that prevents washout of the urea gradient in the inner medullary interstitium (40–42). Mice deficient in UT-B experience a 40% urine concentrating deficiency, and a substantially lowered ability to retain urea in the inner medulla (7). In contrast to UT-As in the inner medullary collecting ducts, which transport urea from the renal tubules into the hyperosmotic interstitium, UT-B mediates net efflux of urea out of the interstitium into the lumen of the vasa recta. Since the descending vasa recta also expresses aquaporins and is therefore highly water permeable (43), it is conceivable that a mismatch in osmolarity between the vasa recta and the interstitium could trigger membrane stretch and thereby upregulate UT-B. The modulation of UT-B by osmotic stress observed in this study therefore appears consistent with the known physiological role of UT-B in the kidney. Further studies would be necessary, however, to know how significant such an effect would be, or to determine the structural changes underlying this modulation.

Methods

Cloning, Expression and Purification of WT and Mutant UT-B. The full-length bovine and human urea transporter genes (AAI05334.1 and BC05039) were subcloned into a modified pFastBac Dual vector (Invitrogen) for baculovirus expression in Sf9 insect cells with a C-terminal TEV protease recognition site followed by an octohistidine tag. Site-directed mutations were introduced by the Quickchange method (Stratagene) or by overlap-extension PCR. The Bac-to-Bac protocol (Invitrogen) was used to produce recombinant baculovirus, and infected Sf9 insect cells were harvested 48–60 h after infection and collected by a low-speed centrifugation step (2,000 g, 10 min). The cells were lysed by sonication and their membranes solubilized with 40 mM n-decyl-β-D-maltoside (DM, Anatrace). UT-B was then purified by affinity chromatography using TALON Metal Affinity Resin (Clontech Inc.). After elution from the resin with 300 mM imidazole, bovine UT-B intended for crystallization was concentrated to 5 mg/ml and partially digested with trypsin protease for 10 min at room temperature in a ratio of 250:1 by weight. The protease digestion reaction was terminated by adding 1 mM PMSF, and the protease-resistant core was subjected to size exclusion chromatography on a Superdex 200 10/300 GL column (GE Health Sciences) preequalized in a buffer of 150 mM NaCl, 20 mM HEPES, pH 7.5, 5 mM β-mercaptoethanol and 36 mM n-octyl-β-D-glucopyranoside. The protein was concentrated to 8 mg/ml as approximated by ultraviolet absorbance. For protein intended for functional assays in liposomes, the trypsin proteolysis step was replaced with a 1 h digestion with 1:10 TEV protease to remove the *C*-terminal His tag, and the size exclusion step was carried out with 4 mM DM.

Crystallization and Structure Determination of UT-B. Crystals of the wild-type UT-B trypsin-resistant core were grown at 4 °C by the sitting-drop vapor diffusion method, where 1.5 μl of protein solution was mixed with an equal volume of crystallization solution containing 25% PEG 400, 50 mM sodium sulfate, 50 mM lithium sulfate, 0.2 mM decyldimethylamine N-oxide (DDAO) and 100 mM Tris, pH 8.0–8.5. Selenourea-bound crystals were obtained by the same method except that selenourea was added to the protein solution to a final concentration of 20 mM before mixing with crystallization solution. Before flash-freezing in liquid nitrogen, the crystals were cryoprotected by gradually increasing the concentration of PEG 400 in the well solution to 35% over 8 h.

X-ray diffraction data were collected at beamlines X25 and X29 of the National Synchrotron Light Source at Brookhaven National Lab, and beamline ID-24 of the Advanced Photon Source at Argonne National Lab. The molecular replacement solution was found for the unliganded structure using a polyalanine search model prepared from the dvUT structure (3K3F) and the program PHASER(44). A partial model was built with phenix.autobuild, and then completed by iterative rounds of manual model building in Coot (45) and refinement with phenix.refine (46) and Refmac (47). In the final stages of refinement, TLSMD was used to compute optimal TLS groups (48), and Molprobity (49) was used to validate geometry. The selenourea-bound structure was solved by molecular replacement using the unliganded structure as a search model, and refinement was carried out by the same methods as for the unliganded structure. Figures of the structures were prepared using PyMol (Schrödinger) and VMD (50).

Reconstitution into Liposomes and Solute Flux Assays. *E. coli* polar lipids in chloroform (Avanti) were dried under argon, and then further dried under vacuum for one hour. Liposomes were formed by rehydrating the lipids at a final concentration of 10 mg/mL in dialysis buffer (100 mM NaCl, 20 mM HEPES pH 7.5) at room temperature for 30 min, and then sonicated to clarity in a bath sonicator. To incorporate protein, the liposomes were incubated first with 10 mM DM for 2 h, followed by addition of protein at a ratio of 1:4000 (w:w). After incubation at room temperature for 30 min, the liposomes were transferred to dialysis cassettes and dialyzed against >500 volumes dialysis buffer for 72 h, with the buffer replaced every 12–24 h. After recovery from the dialysis cassettes, liposomes were frozen in liquid nitrogen and stored at −80 °C until use.

Prior to use in the urea flux assay, liposomes were incubated in 15 mM carboxyfluorescein (CF) overnight at 4 °C. To generate unilamellar vesicles of uniform size, liposomes were subjected to 3 freeze-thaw cycles and then extruded 20 times through a 400 nm filter. External CF dye was removed by passing the liposomes through a PD-10 desalting column (GE Healthcare) equilibrated with internal buffer (200 mM urea, 100 mM NaCl, 20 mM HEPES pH 7.5) and then incubated at room temperature for 30 min. Liposomes were then diluted 1:1 in a stopped flow device at 20 °C with either internal buffer (no urea gradient) or assay buffer (approximately 200 mM NaCl, 20 mM HEPES pH 7.5) with a salt concentration adjusted to identical osmolarity as the internal buffer as measured by a freezing-point depression osmometer (Fiske). The self-quenching of CF fluorescence resulting from shrinkage of the liposomes was monitored by a Fluoromax-3 fluorimeter (Horiba Jobin Yvon) with an excitation wavelength of 492 nm and an emission wavelength of 517 nm. Five traces were collected and averaged for both buffers, and the change in fluorescence for the no-gradient control was subtracted from the assay buffer trace as a background correction. The resulting curves were fitted with double exponentials and solved for the initial rates of flux. Each

experiment was repeated three or four times, using proteoliposomes reconstituted with protein from at least two separate purifications.

Oocyte Uptake Assays. The cRNA of *Bos taurus* UT-B was in vitro transcribed from a pBluescript derivative, purified, and 1 ng (Fig. S7) or 50 ng (Fig. 3*C*) were injected into stage V-VI *Xenopus laevis* oocytes. Oocytes were kept in ND96 (5 mM HEPES, pH 7.6, 96 mM NaCl, 2 mM KCl, 1.8 mM $CaCl_2$, 1 mM $MgCl_2$) for 48 h (Fig. S7) to 72 h (Fig. 3*C*) at 18 °C. For transport measurements, oocytes were transferred into 0.5–1 mL of assay buffer composed of 0.5 X-, 1 X-, or 2 X-strength ND96 supplemented with 168 μM ^{14}C-urea (59.5 Ci/mol; American Radiolabeled Chemicals, Inc.) and incubated for the indicated time at 20 °C. To terminate the uptake reaction, oocytes were washed 4 times with ice-cold assay buffer without radiolabeled urea, individually placed in scintillation vials, solubilized with 10% SDS, and assayed for their ^{14}C-urea content with scintillation counting. Known amounts of ^{14}C-urea were used as standards to transform cpm into pmol.

System Setup and Equilibrium Simulations. The selenourea/UT-B trimer was used as the initial structure. The two bound selenourea molecules were replaced by urea, and the three lipid molecules in the central cavity of the trimer were modeled as three POPC molecules that were subsequently minimized to remove steric clashes. After removing all other detergent molecules, the trimer was embedded into a POPC lipid bilayer (120×120 Å^2), with the membrane normal aligned along the *z* axis. After removing the lipids overlapping with the protein trimer, the system was solvated and ionized with 100 mM NaCl by randomly replacing water molecules with Na^+ or Cl^- ions, resulting in system dimensions of $120 \times 120 \times 90$ Å^3 and approximately 109,000 atoms.

The lipid tails were then "melted" using 5000 steps of energy minimization and 1 ns of constant volume and temperature (NVT) MD simulation at 310 K while all other atoms of the system were fixed, in order to allow the initially ordered lipid tails to maximize their disorder and partially pack against the protein. In the next step, the whole system was simulated for 2 ns under constant pressure and temperature (NPT) conditions while all heavy atoms of the protein and the urea molecules were harmonically restrained ($k = 2$ kcal/mol/Å^2) to allow further relaxation and packing of the lipids against the protein. During this phase, water molecules were prevented from entering the hydrophobic core of the membrane by employing additional constraints. The resulting relaxed configuration of the urea/UT-B system was used as the starting structure for the production simulations described below.

The *apo*-UT-B system was generated by removing the urea molecules from the system. T172S/T334S and T172V/T334V double mutant systems were constructed from the *apo*-UT-B system by mutating the respective residues and minimized for additional 10,000 steps before subjected to MD simulations. The four simulation systems, namely, urea/UT-B, *apo*-UT-B, T172S/T334S, and T172V/T334V, were then each simulated for approximately 60 ns, 100 ns, 45 ns, and 25 ns, respectively, under NPT conditions.

Umbrella Sampling Simulations. In order to reconstruct the potential of mean force (PMF), umbrella sampling (US) simulations were initiated using the 50-ns equilibrated structure from the *apo*-UT-B simulation. 71 umbrella windows of 0.5 Å each were defined along the channel axis, covering a range from $z = -20 - +15$ Å with the origin ($z = 0$) at the center of mass (COM) of the C_α atoms of channel-lining residues (S_i, S_m, and S_o) of each monomer. The starting configuration for each US simulation was generated by adding a urea molecule to each monomer with the position of its carbon atom harmonically ($k = 10$ kcal/mol/Å^2) restrained to the center of the respective window only along the *z* axis. Each starting configuration was separately minimized for 5000 steps and simulated for 5 ns. The restraining potential and the position of the substrate for each monomer were recorded at 0.1-ps intervals. Including only the last 4.5 ns of the US simulations (45,000 data points for each monomer and each window), the weighted histogram analysis method (WHAM) (51, 52) was used to reconstruct the PMF with 0.25 Å resolution for each monomer along with a combined PMF. The quality of the PMF was tested by examining the resulting profile from shorter simulation times (checked for 0.5 ns increments) for each window, clearly indicating convergence (Fig. S8).

Simulation Protocols. All the simulations were performed using NAMD 2.8 with CHARMM27 force field (53) with Φ/ψ cross term map (CMAP) corrections and CHARMM36 all-atom additive parameters for lipids (54). Force field parameters for urea were adopted from Caflisch et al. (55), and water was modeled as TIP3P (56). All production simulations were maintained at 1.0 atm pressure using the Nosé-Hoover Langevin piston method (57, 58) and at 310 K temperature using Langevin dynamics with a damping coefficient of 0.5 ps^{-1} applied to all non-hydrogen atoms. Short-range interactions were cut off at 12 Å with a smoothing function applied after 10 Å, and long-range electrostatic forces were calculated using the particle mesh Ewald (PME) method (59) at a grid density of >1 Å^{-3}. Bonded, non-bonded, and PME calculations were performed at 2-, 2-, and 4-fs intervals, respectively.

ACKNOWLEDGMENTS. Data for this study were measured at beamlines X4A, X4C, X25, and X29 of the National Synchrotron Light Source and the NE-CAT 24ID-C and E at the Advanced Photon Source. This work was supported by the US National Institutes of Health (R01DK088057 to M.Z., T32HL087745 to E.J.L., and R01GM086749, U54GM087519, and P41RR05969 to E.T.). All simulations were performed using NSF XSEDE resources (grant number MCA06N060 to E.T.). M.Z. is grateful to R. MacKinnon for advice and encouragement.

1. Hediger MA, et al. (1996) Structure, regulation and physiological roles of urea transporters. *Kidney Int* 49:1615–1623.
2. Klein JD, Blount MA, Sands JM (2011) Urea transport in the kidney. *Compr Physiol* 1:699–729.
3. Sands JM (2003) Mammalian urea transporters. *Annu Rev Physiol* 65:543–566.
4. Bankir L, Bouby N, Trinh-Trang-Tan MM, Ahloulay M, Promeneur D (1996) Direct and indirect cost of urea excretion. *Kidney Int* 49:1598–1607.
5. Bankir L, Yang B (2012) New insights into urea and glucose handling by the kidney, and the urine concentrating mechanism. *Kidney Int* 81:1179–1198.
6. Fenton RA, et al. (2005) Renal phenotype of UT-A urea transporter knockout mice. *J Am Soc Nephrol* 16:1583–1592.
7. Yang B, Bankir L, Gillespie A, Epstein CJ, Verkman AS (2002) Urea-selective concentrating defect in transgenic mice lacking urea transporter UT-B. *J Biol Chem* 277:10633–10637.
8. Yang B, Verkman AS (2002) Analysis of double knockout mice lacking aquaporin-1 and urea transporter UT-B. Evidence for UT-B-facilitated water transport in erythrocytes. *J Biol Chem* 277:36782–36786.
9. Fenton RA, Chou CL, Stewart GS, Smith CP, Knepper MA (2004) Urinary concentrating defect in mice with selective deletion of phloretin-sensitive urea transporters in the renal collecting duct. *Proc Natl Acad Sci USA* 101:7469–7474.
10. Lei TL, et al. (2011) Role of thin descending limb urea transport in renal urea handling and the urine concentrating mechanism. *Am J PhysiolRenal Physiol* 301:F1251–F1259.
11. Uchida S, et al. (2005) Impaired urea accumulation in the inner medulla of mice lacking the urea transporter UT-A2. *Mol Cell Biol* 25:7357–7363.
12. Ranade K, et al. (2001) Genetic variation in the human urea transporter-2 is associated with variation in blood pressure. *Hum Mol Genet* 10:2157–2164.
13. Garcia-Closas M, et al. (2011) A genome-wide association study of bladder cancer identifies a new susceptibility locus within SLC14A1, a urea transporter gene on chromosome 18q12.3. *Hum Mol Genet* 20:4282–4289.
14. Rafnar T, et al. (2011) European genome-wide association study identifies SLC14A1 as a new urinary bladder cancer susceptibility gene. *Hum Mol Genet* 20:4268–4281.
15. Doran JJ, et al. (2006) Tissue distribution of UT-A and UT-B mRNA and protein in rat. *Am J Physiol Regul Integr Comp Physiol* 290:R1446–R1459.
16. Blount MA, Klein JD, Martin CF, Tchapyjnikov D, Sands JM (2007) Forskolin stimulates phosphorylation and membrane accumulation of UT-A3. *Am J Physiol Renal Physiol* 293:F1308–F1313.
17. Hoffert JD, Pisitkun T, Wang GH, Shen RF, Knepper MA (2006) Quantitative phosphoproteomics of vasopressin-sensitive renal cells: Regulation of aquaporin-2 phosphorylation at two sites. *Proc Natl Acad Sci USA* 103:7159–7164.
18. Zhang C, Sands JM, Klein JD (2002) Vasopressin rapidly increases phosphorylation of UT-A1 urea transporter in rat IMCDs through PKA. *Am J Physiol Renal Physiol* 282:F85–F90.
19. Maciver B, Smith CP, Hill WG, Zeidel ML (2008) Functional characterization of mouse urea transporters UT-A2 and UT-A3 expressed in purified Xenopus laevis oocyte plasma membranes. *Am J Physiol Renal Physiol* 294:F956–F964.
20. Mannuzzu LM, Moronne MM, Macey RI (1993) Estimate of the number of urea transport sites in erythrocyte ghosts using a hydrophobic mercurial. *J Membr Biol* 133:85–97.
21. Levin EJ, Quick M, Zhou M (2009) Crystal structure of a bacterial homologue of the kidney urea transporter. *Nature* 462:757–761.
22. Rousselet G, Ripoche P, Bailly P (1996) Tandem sequence repeats in urea transporters: Identification of an urea transporter signature sequence. *Am J Physiol* 270:F554–F555.
23. Minocha R, Studley K, Saier MH, Jr (2003) The urea transporter (UT) family: Bioinformatic analyses leading to structural, functional, and evolutionary predictions. *Receptors Channels* 9:345–352.
24. Northrup SH, Pear MR, Lee CY, McCammon JA, Karplus M (1982) Dynamical theory of activated processes in globular proteins. *Proc Natl Acad Sci USA* 79:4035–4039.
25. Mathai JC, Zeidel ML (2007) Measurement of water and solute permeability by stopped-flow fluorimetry. *Methods Mol Biol* 400:323–332.
26. Sui H, Han BG, Lee JK, Walian P, Jap BK (2001) Structural basis of water-specific transport through the AQP1 water channel. *Nature* 414:872–878.
27. de Groot BL, Grubmuller H (2001) Water permeation across biological membranes: Mechanism and dynamics of aquaporin-1 and GlpF. *Science* 294(5550):2353–2357.
28. Tajkhorshid E, et al. (2002) Control of the selectivity of the aquaporin water channel family by global orientational tuning. *Science* 296:525–530.

29. Khademi S, et al. (2004) Mechanism of ammonia transport by Amt/MEP/Rh: Structure of AmtB at 1.35 A. *Science* 305:1587–1594.
30. Zheng L, Kostrewa D, Berneche S, Winkler FK, Li XD (2004) The mechanism of ammonia transport based on the crystal structure of AmtB of *Escherichia coli*. *Proc Natl Acad Sci USA* 101:17090–17095.
31. Newby ZE, et al. (2008) Crystal structure of the aquaglyceroporin PfAQP from the malarial parasite *Plasmodium falciparum*. *Nat Struct Mol Biol* 15:619–625.
32. Hub JS, de Groot BL (2008) Mechanism of selectivity in aquaporins and aquaglyceroporins. *Proc Natl Acad Sci USA* 105:1198–1203.
33. Wang Y, Schulten K, Tajkhorshid E (2005) What makes an aquaporin a glycerol channel? A comparative study of AqpZ and GlpF. *Structure* 13:1107–1118.
34. Raunser S, et al. (2009) Oligomeric structure and functional characterization of the urea transporter from *Actinobacillus pleuropneumoniae*. *J Mol Biol* 387:619–627.
35. Zhao D, Sonawane ND, Levin MH, Yang B (2007) Comparative transport efficiencies of urea analogues through urea transporter UT-B. *Biochim Biophys Acta* 1768:1815–1821.
36. Beitz E, Wu B, Holm LM, Schultz JE, Zeuthen T (2006) Point mutations in the aromatic/arginine region in aquaporin 1 allow passage of urea, glycerol, ammonia, and protons. *Proc Natl Acad Sci USA* 103:269–274.
37. Yang B, Verkman AS (1998) Urea transporter UT3 functions as an efficient water channel. Direct evidence for a common water/urea pathway. *J Biol Chem* 273:9369–9372.
38. Klein JD, et al. (2006) Vasopressin increases plasma membrane accumulation of urea transporter UT-A1 in rat inner medullary collecting ducts. *J Am Soc Nephrol* 17:2680–2686.
39. Stewart GS, Thistlethwaite A, Lees H, Cooper GJ, Smith C (2009) Vasopressin regulation of the renal UT-A3 urea transporter. *Am J Physiol Renal Physiol* 296:F642–F648.
40. Kokko JP, Rector FC, Jr (1972) Countercurrent multiplication system without active transport in inner medulla. *Kidney Int* 2:214–223.
41. Layton AT (2007) Role of UTB urea transporters in the urine concentrating mechanism of the rat kidney. *Bull Math Biol* 69:887–929.
42. Stephenson JL (1972) Concentration of urine in a central core model of the renal counterflow system. *Kidney Int* 2:85–94.
43. Pallone TL, Kishore BK, Nielsen S, Agre P, Knepper MA (1997) Evidence that aquaporin-1 mediates NaCl-induced water flux across descending vasa recta. *Am J Physiol* 272:F587–F596.
44. McCoy AJ, et al. (2007) Phaser crystallographic software. *J Appl Crystallogr* 40:658–674.
45. Emsley P, Cowtan K (2004) Coot: Model-building tools for molecular graphics. *Acta Crystallogr D Biol Crystallogr* 60:2126–2132.
46. Adams PD, et al. (2010) PHENIX: A comprehensive Python-based system for macromolecular structure solution. *Acta Crystallogr D Biol Crystallogr* 66:213–221.
47. Dodson EJ, Winn M, Ralph A (1997) Collaborative Computational Project, number 4: Providing programs for protein crystallography. *Methods Enzymol* 277:620–633.
48. Painter J, Merritt EA (2006) Optimal description of a protein structure in terms of multiple groups undergoing TLS motion. *Acta Crystallogr D Biol Crystallogr* 62:439–450.
49. Chen VB, et al. (2010) MolProbity: All-atom structure validation for macromolecular crystallography. *Acta Crystallogr D Biol Crystallogr* 66:12–21.
50. Humphrey W, Dalke A, Schulten K (1996) VMD: Visual molecular dynamics. *J Mol Graph* 14(1):33–38–27–38.
51. Kumar S, Bouzida D, Swendsen RH, Kollman PA, Rosenberg JM (1992) The weighted histogram analysis method for free-energy calculations on biomolecules. 1. The method. *J Comput Chem* 13:1011–1021.
52. Roux B, Souaille M (2001) Extension to the weighted histogram analysis method: Combining umbrella sampling with free energy calculations. *Comput Phys Commun* 135:40–57.
53. Mackerell AD, Feig M, Brooks CL (2004) Extending the treatment of backbone energetics in protein force fields: Limitations of gas-phase quantum mechanics in reproducing protein conformational distributions in molecular dynamics simulations. *J Comput Chem* 25:1400–1415.
54. MacKerell AD, et al. (2010) Update of the CHARMM all-atom additive force field for lipids: Validation on six lipid types. *J Phys Chem B* 114:7830–7843.
55. Caflisch A, Karplus M (1999) Structural details of urea binding to barnase: A molecular dynamics analysis. *Struct Fold Des* 7:477–488.
56. Jorgensen WL, Chandrasekhar J, Madura JD, Impey RW, Klein ML (1983) Comparison of simple potential functions for simulating liquid water. *J Chem Phys* 79:926–935.
57. Feller SE, Zhang YH, Pastor RW, Brooks BR (1995) Constant-pressure molecular-dynamics simulation—the Langevin piston method. *J Chem Phys* 103:4613–4621.
58. Martyna GJ, Tobias DJ, Klein ML (1994) Constant-pressure molecular-dynamics algorithms. *J Chem Phys* 101:4177–4189.
59. Darden T, York D, Pedersen L (1993) Particle mesh Ewald—an N.Log(N) method for Ewald sums in large systems. *J Chem Phys* 98:10089–10092.